Fabrication, Characterization, and Analysis of a DRIE CMOS-MEMS Gyroscope

Huikai Xie and Gary K. Fedder

Abstract—A gyroscope with a measured noise floor of $0.02°/s/Hz^{1/2}$ at 5 Hz is fabricated by post-CMOS micromachining that uses interconnect metal layers to mask the structural etch steps. The 1×1 mm lateral-axis angular rate sensor employs in-plane vibration and out-of-plane Coriolis acceleration detection with on-chip CMOS circuitry. The resultant device incorporates a combination of 1.8-μm-thick thin-film structures for springs with out-of-plane compliance and 60-μm-thick bulk silicon structures defined by deep reactive-ion etching for the proof mass and springs with out-of-plane stiffness. The microstructure is flat and avoids excessive curling, which exists in prior thin-film CMOS-microelectromechanical systems gyroscopes. Complete etch removal of selective silicon regions provides electrical isolation of bulk silicon to obtain individually controllable comb fingers. Direct motion coupling is observed and analyzed.

Index Terms—CMOS-microelectromechanical systems (MEMS), deep reactive-ion-etched (DRIE), electrical isolation, gyroscope, integrated gyroscope, single-crystal silicon.

I. INTRODUCTION

COMMERCIAL microelectromechanical systems (MEMS) inertial sensors are extremely attractive because of their miniaturization with rate-grade performance at low cost. For many niche applications, there is a need for custom inertial sensors, with a trend toward greater sensor fusion on chip. To meet low-cost custom design needs, there has been recent progress on CMOS-MEMS inertial sensors [1], [2]. Vibratory-rate gyroscopes based on the Coriolis effect benefit from robust microstructures, where single-crystal silicon structures are advantageous. In this paper, we report an integrated deep reactive-ion-etched (DRIE) silicon CMOS-MEMS lateral-axis gyroscope with in-plane vibration and out-of-plane Coriolis acceleration sensing. Prior work on DRIE silicon CMOS micromachining resulted in fabrication of a z-axis accelerometer [3]. The process combines a backside deep silicon etch step with maskless post-CMOS micromachining [4] to achieve thick, flat silicon microstructures. CMOS-MEMS advantages of wiring flexibility within structures, structures with different thicknesses, low parasitic capacitance, three-dimensional electrostatic actuation and capacitive sensing are maintained.

The on-chip interface circuitry enables high sensitivity and low noise with moderate device size.

There are several types of gyroscopes including traditional spinning wheels, ring lasers and vibratory structures. Most of MEMS gyroscopes are vibratory type that is more suitable for microfabrication processes. The first silicon micromachined vibratory gyroscope was proposed by Draper Lab in 1986 [5], [6]. After that, various fabrication technologies, structural designs and drive/sense mechanisms have been investigated. During the early 1990s, bulk micromachining and metal electroforming were mostly used to form large masses. Draper Lab's single-crystal-silicon-on-glass tuning fork gyroscope demonstrated a resolution of $1.5°/s$ in a 60-Hz bandwidth in 1993 [7]. The University of Michigan's metal electroforming vibrating ring gyroscope achieved a resolution of $0.5°/s$ in a 10-Hz bandwidth in 1994 [8]. In the mid-90s, surface micromachined gyroscopes enabled the integration of read-out circuits integrated on the same chip. The University of California Berkeley's surface micromachined z-axis gyroscope achieved a noise floor of $1°/s/Hz^{1/2}$ in 1996 [9] which was improved to $0.2°/s/Hz^{1/2}$ in 1997 [10]. Carnegie-Mellon demonstrated both lateral-axis and z-axis gyroscopes with noise floor of about $0.5°/s/Hz^{1/2}$ [1], [2] using a maskless post-CMOS micromachining process [4]. Analog Devices, Inc., reported a z-axis gyroscope with $0.05°/s/Hz^{1/2}$ noise floor in 2002 [11] that is commercial available now.

Bulk micromachined gyroscopes also made noticeable progress after 1995. The microgyroscope with a clover-leaf shape and a metal post attached to the center, developed at JPL, showed a noise floor of $0.1°/s/Hz^{1/2}$ in 1997 [12]. Murata reported a deep RIE gyroscope with decoupling of the sense and drive modes and a resolution of $0.07°/s$ at bandwidth of 10 Hz in 1999 [13].

Design tradeoffs drive the choice between bulk and surface micromachining for gyroscopes. Prior bulk micromachined gyroscopes have large mass but no on-chip read-out electronics and require Si-Si and/or Si-glass anodic bonding and two-side alignment. Surface micromachined gyroscopes have integrated read-out electronics but small mass, and they can suffer from thin-film residual stress, squeeze-film damping, and sacrificial layer release problems.

The ideal case is to combine the advantages of the two micromachining processes. Both Bosch and Samsung explored the possibility to fabricate gyroscopes using the combination of bulk and surface micromachining (i.e., mixed technology) [14]–[16]. However, the mixed technology still suffers from sacrificial layer release and squeeze-film damping problems and often requires expensive SOI wafers. Polysilicon-refilled

		Form Approved OMB No. 0704-0188

Report Documentation Page

Form Approved
OMB No. 0704-0188

Public reporting burden for the collection of information is estimated to average 1 hour per response, including the time for reviewing instructions, searching existing data sources, gathering and maintaining the data needed, and completing and reviewing the collection of information. Send comments regarding this burden estimate or any other aspect of this collection of information, including suggestions for reducing this burden, to Washington Headquarters Services, Directorate for Information Operations and Reports, 1215 Jefferson Davis Highway, Suite 1204, Arlington VA 22202-4302. Respondents should be aware that notwithstanding any other provision of law, no person shall be subject to a penalty for failing to comply with a collection of information if it does not display a currently valid OMB control number.

1. REPORT DATE **JUN 2003**	2. REPORT TYPE	3. DATES COVERED **00-00-2003 to 00-00-2003**
4. TITLE AND SUBTITLE **Fabrication, Characterization, and Analysis of a DRIE CMOS-MEMS Gyroscope**		5a. CONTRACT NUMBER
		5b. GRANT NUMBER
		5c. PROGRAM ELEMENT NUMBER
6. AUTHOR(S)		5d. PROJECT NUMBER
		5e. TASK NUMBER
		5f. WORK UNIT NUMBER
7. PERFORMING ORGANIZATION NAME(S) AND ADDRESS(ES) **University of Florida,Department of Electrical and Computer Engineering,Gainesville,FL,32611**		8. PERFORMING ORGANIZATION REPORT NUMBER
9. SPONSORING/MONITORING AGENCY NAME(S) AND ADDRESS(ES)		10. SPONSOR/MONITOR'S ACRONYM(S)
		11. SPONSOR/MONITOR'S REPORT NUMBER(S)
12. DISTRIBUTION/AVAILABILITY STATEMENT **Approved for public release; distribution unlimited**		
13. SUPPLEMENTARY NOTES		
14. ABSTRACT		
15. SUBJECT TERMS		

16. SECURITY CLASSIFICATION OF:			17. LIMITATION OF ABSTRACT	18. NUMBER OF PAGES **10**	19a. NAME OF RESPONSIBLE PERSON
a. REPORT **unclassified**	b. ABSTRACT **unclassified**	c. THIS PAGE **unclassified**			

Standard Form 298 (Rev. 8-98)
Prescribed by ANSI Std Z39-18

isolation trench technique has also been used to fabricate single-crystal silicon (SCS) gyroscopes [17], [18], but the degree of CMOS-compatibility and design flexibility are still concerns.

In this paper, we present a lateral-axis vibratory gyroscope that has both single-crystal silicon (SCS) microstructures and full CMOS-compatibility. Compared to the existing gyroscopes, the reported gyroscope is fabricated using a unique DRIE CMOS-MEMS process [3]. It integrates single-crystal silicon based-sensor structures, CMOS circuits, thin beams ($< 5\ \mu$m), and thick structures ($> 45\ \mu$m) on a single chip without the use of wafer-to-wafer bonding, SOI wafers, or two side alignment. Since z-axis gyroscopes have been extensively fabricated using both in-plane actuation and sensing, this work is focused on the feasibility to realize lateral-axis gyroscope using out-of-plane sensing. Then monolithic three-axis integrated gyroscopes can be achieved.

First, the fabrication process and its unique vertical-axis sensing/actuation capability are introduced. Next, two possible gyroscope topology designs with vertical sensing or actuation are compared and evaluated by using a simplified three-dimensional (3-D) comb-drive model. Then, a finite-element simulation is performed on the chosen topology design. Next, the fabrication and characterization of the device are discussed.

II. DRIE Silicon CMOS-MEMS Process

The DRIE silicon post-CMOS micromachining process flow and a fabricated example microstructure are shown in Fig. 1. First, a backside DRIE silicon etch is performed [Fig. 1(a)(i)]. This backside etch step thins the silicon layer to between 50 to 80-μm- thick for subsequent front-side creation of the microstructures. Next, a front-side reactive-ion etch of the dielectric layers forms structural sidewalls masked by the top CMOS metal layer [Fig. 1(a)(ii)]. Then, another DRIE silicon etch extends the structural sidewalls into the underlying silicon [Fig. 1(a)(iii)]. Because of the high aspect ratio, lateral-axis compliant springs can be made by using narrow, thick SCS beams, as shown in Fig. 2(a). The final step is a short timed isotropic silicon etch [Fig. 1(a)(iv)], which provides a specific undercut of the exposed silicon sidewalls. This undercut can electrically isolate specific bulk silicon structures, as illustrated in Fig. 1(b), or to realize z-axis compliant springs, as shown in Fig. 2(b).

III. Gyroscope Design

When a structure is vibrating in a rotating reference frame, a Coriolis acceleration arises and is proportional to the rotation rate $\vec{\Omega}$ and the vibration velocity $\vec{V}$, i.e.

$$\vec{a}_{co} = 2 \cdot \vec{\Omega} \times \vec{V}. \tag{1}$$

The Coriolis acceleration is orthogonal to both the vibration velocity and rotation rate. Therefore, either out-of-plane vibratory actuation or out-of-plane acceleration sensing is required for detection of lateral-axis (in-plane) rotational rate.
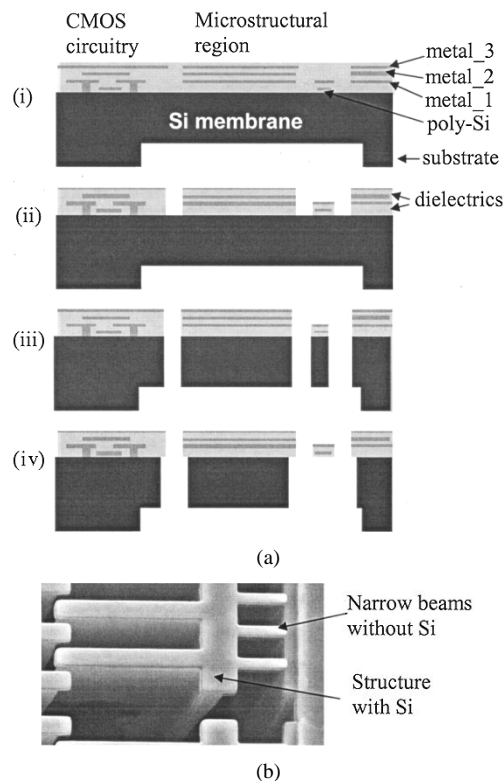

Fig. 1. DRIE CMOS-MEMS process in which interconnect metal layers are used as etching mask. (a) Cross-sectional view of the process steps: (i) backside deep Si etch. (ii) Anisotropic oxide etch. (iii) Deep Si etch for release. (iv) Si undercut. (b) Micrograph of a fabricated comb drive which has electrically isolated silicon electrodes.
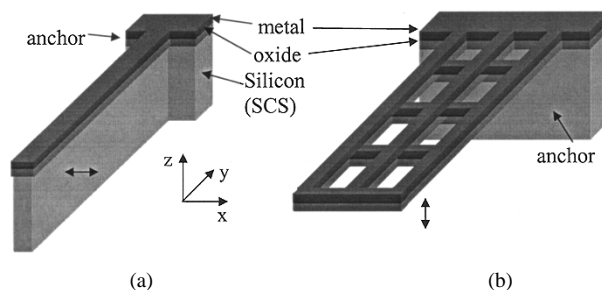

Fig. 2. Spring designs. (a) Lateral-axis SCS spring. (b) Vertical-axis thin-film spring (no SCS layer).

A. Electrode Design for Vertical-Axis Sensing and Actuation

Vertical-axis motion sensing is realized by using the multiple metal layers in the comb fingers. As shown in Fig. 3(a), there are two electrically isolated electrodes in the stator fingers. The two capacitors, C_1 and C_2, change values in opposite ways with the z-axis motion of the rotor finger, resulting in a differential capacitive divider. The silicon layer is used as a mechanical support. V_{m+} and V_{m-} are balanced modulation voltages.

Note that C_1 is not equal to C_2, which will cause a large dc offset. This dc offset actually can be cancelled out by using the wiring flexibility provided by the CMOS-MEMS processes. As shown in Fig. 3(b), two groups of comb fingers have the same cross-section, but their rotors and stators are swapped. If the rotors move down, the top capacitor C_2 of Group A and bottom capacitor C_1' of Group B increase while the bottom capacitor C_1 of Group A and top capacitor C_2' of Group B decrease. If the top
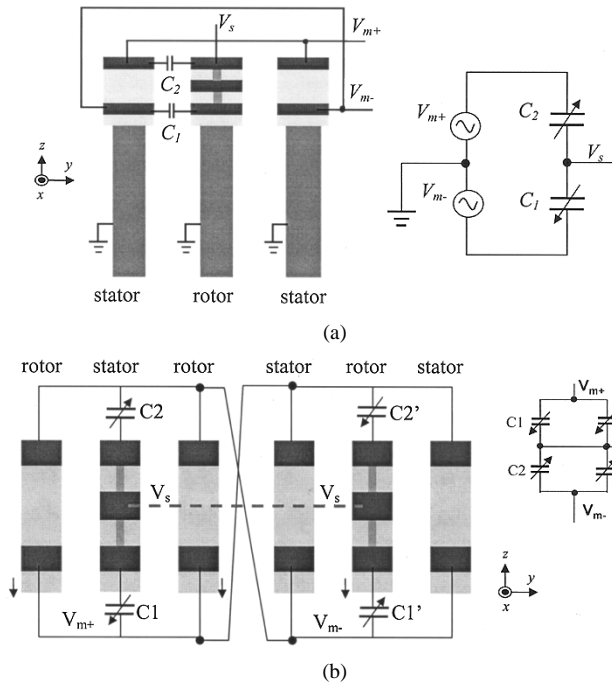
Fig. 3. Z-axis sensing principle. (a) Differential sidewall capacitive bridge. (b) Sidewall capacitance offset cancellation (SCS layer is not shown).
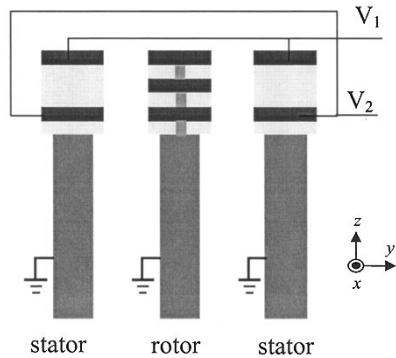

Fig. 4.   Combined x-axis/z-axis actuation principle.

Fig. 5.   Comparison of vertical sensing and vertical actuation.

B. Choosing Between Vertical Actuation and Sensing

Lateral-axis gyroscopes must implement either vertical sensing or vertical actuation, according to (1). Topologies representative of the two alternatives are shown in Fig. 5. For the vertical sensing topology [Fig. 5(a)], an SCS proof mass is centered inside a rigid SCS frame through four groups of z-compliant, thin-film spring beams. So, a z-axis accelerometer is formed. The SCS frame is also connected to the substrate through four y-axis SCS drive springs. Upon operation, the SCS frame together with the z-axis accelerometer vibrates along the y-axis and an x-axis external rotation can be detected. Thus, the drive and sense modes are decoupled through the use of the SCS frame. This also applies to the vertical actuation topology [Fig. 5(b)], where an SCS frame together with an x-axis accelerometer vibrates in the z-axis and a y-axis external rotation can be detected.

The major distinction between topologies is the orientation of comb fingers. The orientation of the lateral comb fingers must be orthogonal to the input rate axis. The orientation of vertical comb fingers has no such constraint. The vertical comb fingers may be oriented along the $x-$, $y-$, $x - y$ axis or any arbitrary direction in the $x - y$ plane. The topology shown in Fig. 5(a) has x-axis actuation and z-axis sensing. A y-axis electrostatic force will be also generated since comb fingers always have some lateral offset even though very small in DRIE structures. This y-axis force produces a y-axis vibration acting on the central z-axis accelerometer. In order to minimize the sensitivity of the z-axis accelerometer to this undesired vibration, the z-axis comb fingers of the accelerometer orient along the y-axis.

The topology shown in Fig. 5(b) employs z-axis actuation and y-axis sensing. In this case, any lateral offset in the drive fingers

and bottom electrodes of Group A are, respectively, connected to the bottom and top electrodes of Group B, then increasing C_2 and C_1', and decreasing C_1 and C_2' are grouped together, respectively, to form a capacitive bridge. Since each branch of the bridge has a top capacitor and a bottom capacitor, the sum of the capacitances of each branch is equal at the rest position, i.e., $C_1 + C_2' = C_2 + C_1'$ at $z = 0$.

The operational principle of z-axis electrostatic comb actuation is shown in Fig. 4. It is actually a combined x-axis/z-axis actuator in which the stator fingers have two electrodes and the rotor fingers have one electrode. A z-axis force is generated when a voltage (e.g., V_1) is applied to one stator electrode, with the other electrode grounded (e.g., $V_2 = 0$). When the same voltage (i.e., $V_1 = V_2$) is applied to both electrodes in the stator fingers, the net electrostatic force only exists in the x-direction. Note that as shown in Fig. 4 the z-axis actuation range is limited to the thickness of the aluminum/oxide composite layer.
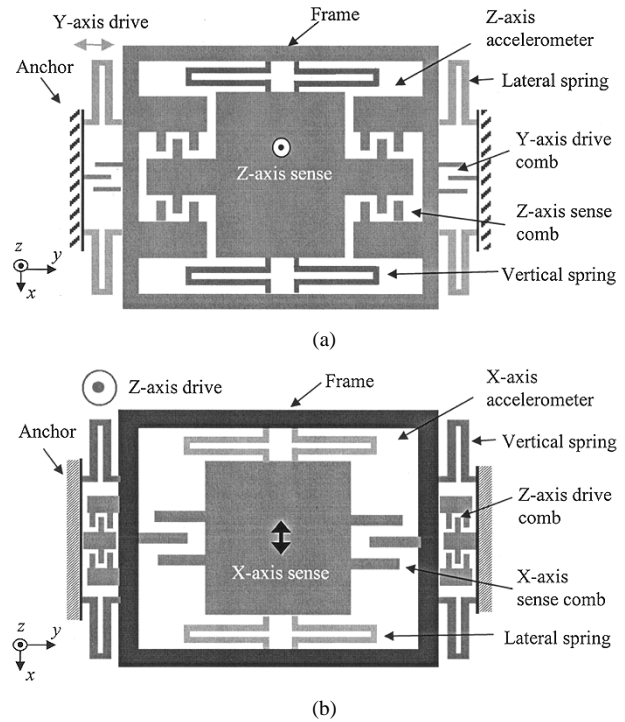
l: overlap of comb fingers
Δg_0: lateral offset due to processing
z_0: vertical offset due to processing
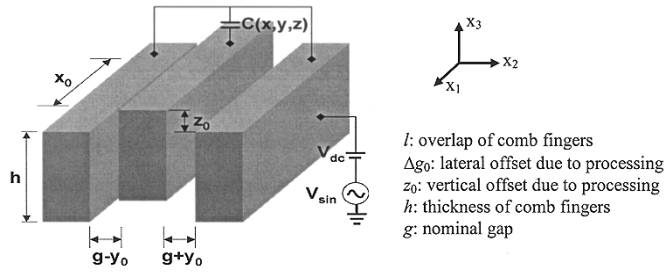*h*: thickness of comb fingers
g: nominal gap

Fig. 6.   Comb finger model for 3-D electrostatic force analysis.

will cause a small y-axis vibration. Minimizing the accelerometer sensitivity to the y-axis vibration dictates sense fingers oriented along the y-axis.

Lateral spring beams have silicon underneath, and thus they are flat and have good comb-finger alignment and high stiffness ratio between the $x, y,$ and z axes. Therefore, the gyroscope shown in Fig. 5(a), which has lateral-axis drive springs, is expected to have a very stable excitation vibration with little cross-axis coupling. Likewise, the inner accelerometer in Fig. 5(b), which has lateral-axis sense springs, is expected to have low cross-axis sensitivity.

In order to compare the performance of these two topologies, the electrostatic force must be analyzed. Fig. 6 shows a three-dimensional comb finger model with presumed lateral offset, Δg_0, and vertical offset, z_0. Coordinate set (x_1, x_2, x_3) is used to distinguish it from the coordinate set (x, y, z) in Fig. 5. For this first-order analysis, the parallel-plate approximation is used and fringing effects are ignored. The capacitance of the comb finger is then

$$C(x_1, x_2, x_3) = \varepsilon_0(h - z_0 - x_3)$$
$$\times \left(\frac{l_0 + x_1}{g + \Delta g_0 + x_2} + \frac{l_0 + x_1}{g - \Delta g_0 - x_2} \right). \quad (2)$$

The capacitance gradients, $dC/dx_1, dc/dx_2,$ and dc/dx_3, are readily derived from (2). Notice the x-axis in Fig. 5(b) is along the orientation of the drive comb fingers. The sensitivity of a gyroscope is proportional to mechanical sensitivity and capacitance gradient, as shown in the following equations, where it is assumed that $\Delta g_0 \ll g$. For the vertical sensing topology [Fig. 5(a)], the output voltage can be expressed as

$$\frac{V^{vs}}{\Omega_x} = \frac{\frac{ma_c}{\Omega_x}}{k_{z,\mathrm{drv}}^{vs}} \cdot \frac{dC}{dx_3} \cdot \frac{N}{2} \cdot V_m, \quad (3)$$

where Ω_x is the external rotation, m is the proof mass, a_c is Coriolis acceleration, $k_{z,\mathrm{drv}}^{vs}$ is the spring constant of the drive mode, N is the number of the drive comb fingers and V_m is the amplitude of the modulation voltage. Substituting (1) and (2) into the above equation yields

$$\frac{V^{vs}}{\Omega_x} = \frac{2m\omega_d^{vs}y_d}{k_{z,\mathrm{drv}}^{vs}} \cdot \frac{\varepsilon_0 l_0}{g} \cdot N \cdot V_m \quad (4)$$

where ω_d^{vs} and y_d are respectively the resonant frequency and vibration amplitude of the drive mode. Likewise, the output

voltage for the vertical drive topology [Fig. 5(b)] can be written as

$$\frac{V^{vd}}{\Omega_y} = \frac{2m\omega_d^{vd}z_d}{k_{x,\mathrm{drv}}^{vd}} \cdot \frac{\varepsilon_0(h - z_0)l_0}{g^2} \cdot N \cdot V_m \quad (5)$$

where Ω_y is the external rotation, and ω_d^{vd}, z_d, and $k_{x,\mathrm{drv}}^{vd}$ are, respectively, the resonant frequency, vibration amplitude, and spring constant of the drive mode of the vertical drive topology. To compare the sensitivity, we may assume the two topologies have the same resonant frequencies and same spring constants for the drive modes. Thus, the sensitivity ratio of the two competing topologies is

$$\frac{\frac{V^{vs}}{\Omega_x}}{\frac{V^{vd}}{\Omega_y}} = \frac{g}{h - z_0} \cdot \frac{y_d}{z_d}. \quad (6)$$

Typically, $g = 3\ \mu$m, $h = 60\ \mu$m and $z_0 = 0$. For the vertical sense topology, the drive motion is along the longitudinal direction of the comb fingers, so a vibration amplitude of $20\ \mu$m or more can be achieved. For the vertical drive topology, the drive motion is out-of-plane and limited by the thickness of the aluminum/oxide composite layer, which is about $5\ \mu$m. Therefore, the vertical drive topology has about four times higher sensitivity than the vertical sense topology.

The direct drive motion also can couple to the sense mode through the drive springs, which will have cross-axis stiffness coefficients $k_{zx,\mathrm{drv}}^{vd}$ for the vertical drive topology and $k_{yz,\mathrm{drv}}^{vs}$ for the vertical sense topology. This type of coupled motion is also referred as quadrature error [9]. The quadrature errors for the two topologies are

$$z_{q,\mathrm{sense}}^{vs} = \frac{F_{y,\mathrm{drv}}^{vs}}{k_{yz,\mathrm{drv}}^{vs}} = \frac{m_{\mathrm{drv}}}{k_{yz,\mathrm{drv}}^{vs}} \cdot \omega_d^2 \cdot y_d \quad (7)$$

$$x_{q,\mathrm{sense}}^{vd} = \frac{F_{z,\mathrm{drv}}^{vd}}{k_{zx,\mathrm{drv}}^{vd}} = \frac{m_{\mathrm{drv}}}{k_{zx,\mathrm{drv}}^{vd}} \cdot \omega_d^2 \cdot z_d \quad (8)$$

where m_{drv} is the whole structure mass, and y_d and z_d are the drive amplitudes for the respective topologies. Therefore, the quadrature ratio of the two topologies is given by

$$\frac{z_{q,\mathrm{sense}}^{vs}}{x_{q,\mathrm{sense}}^{vd}} = \frac{k_{zx,\mathrm{drv}}^{vd}}{k_{yz,\mathrm{drv}}^{vs}} \cdot \frac{y_d}{z_d}. \quad (9)$$

Compared to the silicon lateral springs, the thin-film vertical springs will have much smaller cross-axis stiffness coefficient due to the curling and small thickness, i.e., $k_{zx,\mathrm{drv}}^{vd} \ll k_{yz,\mathrm{drv}}^{vs}$, which implies that the vertical sense topology has much smaller quadrature error according to (9). However, this advantage of the vertical sense topology will be compensated by the fact that y_d is about three times larger than z_d as discussed above. According to (6), large y_d is required to increase the sensitivity of the vertical sense topology.

Cross-sensitivity is another important performance measure of a gyroscope. According to (1), the cross-axis rotation sensitivity is caused by off-axis motion along the rotation sense axis, i.e., the x-axis in Fig. 5(a), and the y-axis in Fig. 5(b). There are two sources of off-axis motion. Similar to the quadrature motion shown in (7) and (8), the cross-axis motion coupling will also be

TABLE I
COMPARISON OF THE TWO TOPOLOGY DESIGNS

Parameter	Vertical Sense	Vertical Drive	Parameter		Vertical Sense	Vertical Drive
Sensitivity		greater	Allowable drive amplitude		>25μm	5μm
Cross-sensitivity	much smaller		Drive voltage		40V	35 V
Quadrature	Smaller		Vibration stability		high	low
Resolution	Same	same	Q-factor (in air)	Drive mode	45	30
				Sense mode	15	5

present in the x-direction of the vertical sensing topology and in the y-direction of the vertical drive topology. Again, because of the curling and small thickness of the thin-film vertical springs, the vertical drive topology has much larger coupling motion.

The other off-axis motion source is from the direct electrostatic drive force. According to the comb drive designs shown in Fig. 5, both topologies have this off-axis motion along the transverse direction (x_2 in Fig. 6) of the drive comb fingers. The amplitudes of this motion for the two topologies and their ratio can be expressed as

$$x^{vs} = \frac{F_x^{vs}}{k_{x,\mathrm{drv}}^{vs}} = \frac{1}{2}\frac{dc}{dx_2}\frac{V^2}{k_{x,\mathrm{drv}}^{vs}}$$
$$= \frac{2\varepsilon_0(h-z_0)(l_0^{vs})(\Delta g_0)^{vs}}{g^3}\frac{V^2}{k_{x,\mathrm{drv}}^{vs}} \quad (10)$$

$$y^{vd} = \frac{F_y^{vd}}{k_{y,\mathrm{drv}}^{vd}} = \frac{1}{2}\frac{dc}{dx_2}\frac{V^2}{k_{y,\mathrm{drv}}^{vd}}$$
$$= \frac{2\varepsilon_0(h-z_0)(l_0^{vd})(\Delta g_0)^{vd}}{g^3}\frac{V^2}{k_{y,\mathrm{drv}}^{vd}} \quad (11)$$

$$\frac{x^{vs}}{y^{vd}} = \frac{l_0^{vd}}{l_0^{vs}}\frac{(\Delta g_0)^{vd}}{(\Delta g_0)^{vs}}\frac{k_{x,\mathrm{drv}}^{vs}}{k_{y,\mathrm{drv}}^{vd}} \quad (12)$$

where l_0 is about 60 μm in the vertical actuation case but about 5 μm in the vertical sensing case, and Δg_0 in the vertical actuation case is about one order of magnitude greater than that in the vertical sensing case because of the thick, flat x-axis spring beams. The stiffness ratio in (12) may vary from 10 to 100. Overall, the vertical actuation topology has about 60- to 80-dB greater cross-sensitivity than the vertical sensing if only the off-axis drive motion is considered.

The performance comparison of these two topologies is summarized in Table I. The table shows that the vertical drive topology has higher sensitivity, but rest of the parameters are favorable to the vertical sense topology. Therefore, the vertical-axis sense lateral-axis drive topology is chosen for best performance.

The detailed topology is shown in Fig. 7, which primarily consists of a x-axis resonator and a z-axis accelerometer. An x-axis capacitive sensor, a y-axis actuator and a combined x-axis/z-axis actuator also are integrated to control the excitation vibration and compensate the coupled motion. All the sensors and actuators are in the form of comb drives with the geometric parameters listed in Table II.

The x-axis capacitive sensor, used to detect the drive motion, has separate groups of comb fingers located at each of the
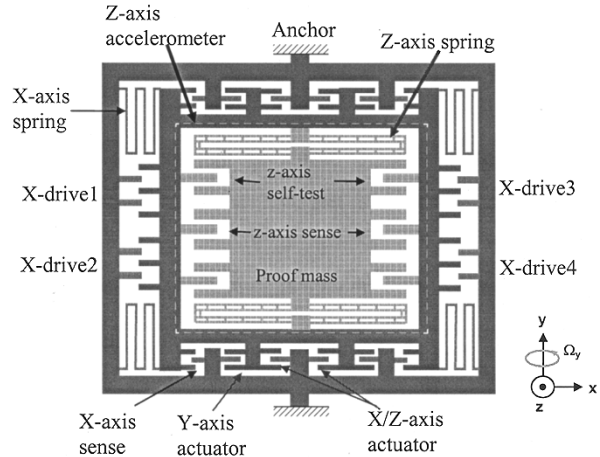

Fig. 7. Topology of the lateral-axis DRIE gyroscope.

four corners to form a differential capacitive sensing bridge. A unity-gain buffer is required to drive capacitance of the output bond pad. In the envisioned full system, the detected signal is amplified and fed back to the x-axis actuators to form an oscillator. However, in the experiments, the gyroscope is driven open loop. The y-axis actuator uses the parallel-plate electrostatic force existing in the comb fingers.

In order to balance the excitation vibration in the x-y plane, the primary x-axis drive is divided into four groups through the electrical isolation of silicon. For instance, if the vibrating structure is imbalanced and rotates clockwise, the voltages on x-drive1 and x-drive4 can be increased to balance the rotation.

The main design parameters are listed in Table III. The gyroscope operates at atmospheric pressure. Vacuum packaging will not be employed since microstructures can be easily damaged in vacuum without special protection. Vacuum packaging will also drastically increase the cost. The quality factors, Q, listed in Table III, are measured in air. The drive mode has larger Q than the sense mode because the drive comb fingers have only 3-μm overlaps while the sense comb fingers have 100-μm overlaps. Furthermore, the drive mode is designed to be slightly lower than the sense mode, so that the scale factor of the sensor will have very little change by the resonant frequency variations.

IV. MODAL SIMULATION

The structure shown in Fig. 7 consists of multiple layers and hundreds of comb fingers. It requires enormous computing power and time if a finite-element analysis is performed on the full structure. In determination of the mechanical modes of the

TABLE II
GEOMETRIC PARAMETERS OF COMB DRIVES OF THE GYROSCOPE

		finger width	finger length	# of fingers	overlap	gap	capacitance gradient or force
Sense mode	sense comb	4 μm	99 μm	41×8	95 μm	2.1 μm	83 aF/nm
	self-test comb	2 μm	15 μm	7×10	13.5 μ m	2.1 μm	1.3 nN/V^2
Drive mode	x-axis drive	3μm	22μm	67×4	2μm	1.8μm	16nN/V^2
	x-axis sense	3μm	30μm	23×4	10μm	1.8μm	0.13fF/μm
	y-axis drive	3μm	70μm	19×4	50μm	2.1μm	53nN/V^2
	x-axis/z-axis drive	3.6μm	80μm	19×4	60μm	2.1μm	4.1nN/V^2 (x) 6.3nN/V^2 (z)

TABLE III
DESIGN DATA SHEET

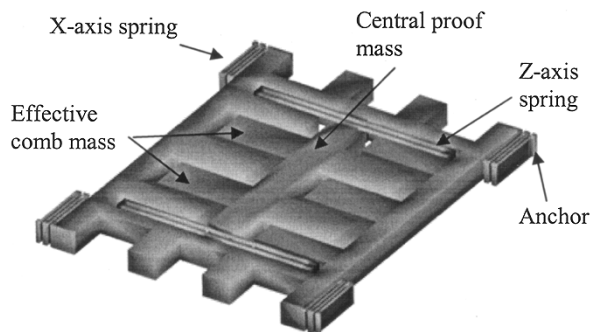|	Resonant Frequency	Spring Constant	Q-factor (in air)	Vibration Amplitude
Drive Mode	3.9 kHz	51 N/m	45	5 μm
Sense Mode	4.8 kHz	49 N/m	15	1.2 pm/(°/s)

Fig. 8. Coventorware 3-D solid model of the gyroscope.

TABLE IV
FIRST FOUR MODES OF THE Y-AXIS GYROSCOPE

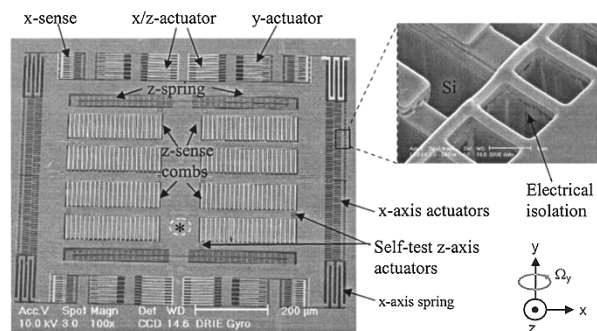| Mode #	1	2	3	4
Resonance (kHz)	3.91	4.84	4.94	8.13
Description	x-axis drive	z-axis sense	θ_y sense	θ_x sense

Fig. 9. SEM of the y-axis DRIE gyroscope. The asterisk marks the spot for the optical motion measurement shown in Fig. 10.

V. FABRICATION

The CMOS chips were fabricated through the Austria Microsystems 0.6-μm three-metal CMOS process. The post-CMOS processing sequence shown in Fig. 1 was used to fabricate the device. The DRIE silicon etch steps were performed with a surface technology systems inductively coupled plasma etching system. The DRIE process parameters are set to a 12-s etch cycle time with 130 sccm SF$_6$, 13 sccm O$_2$, 23-mT chamber pressure, 600-W coil power and 12-W platen power, and 8-s passivation cycle time with 85 sccm C$_4$F$_8$, 12-mT chamber pressure, 600-W coil power, and no platen power. The etch rate is about 2.5 μm/min.

The thickness of the silicon membrane was about 60 μm and controlled by timing. A white light profilometer (NT2000) was used to measure the etching depth. Thus, the silicon membrane thickness could be calculated because the chip thickness was measured before the post-CMOS processing.

The dielectric etch was performed in a PlasmaTherm 790 RIE system with 22.5 sccm CHF$_3$, 16 sccm O$_2$, 100-W RF power and 125-mT chamber pressure. The timing of the final silicon undercut is very critical. Complete silicon undercut must be ensured for the short, narrow beams for electrical isolation. At the same time, the silicon underneath comb fingers and lateral-axis spring beams must remain intact to maintain the flatness of the whole structure. The thickness of the thin-film structures was 4.9 μm that was measured on test beams using scanning electron micrograph.

A scanning electron micrograph (SEM) of a fabricated device is shown in Fig. 9. The drive fingers are located on the two sides of the device. The total area of the microstructure is 0.85 × 1.0 mm. The z-sense spring beams are single-turn and
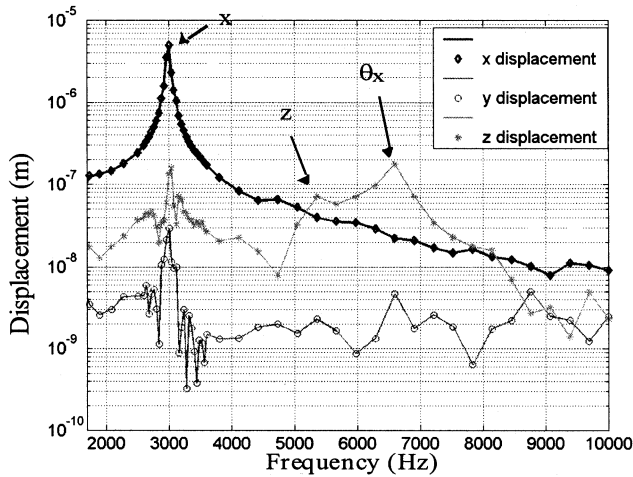
structure, the comb fingers simply contribute effective mass. Fig. 8 shows the 3-D solid model generated by Coventorware [19], in which the comb fingers are eliminated and modeled as solid plates. The thickness of the structure is 55 μm. However, the z-axis spring beams are composed of only CMOS interconnect layers and are 4.9-μm thick. The x-axis drive spring beams are 3.9-μm wide with a 0.9-μm silicon undercut on each side.

The first four modes obtained from the Coventorware FEM simulation isl isted in Table IV. The primary drive and sense modes are 3.9 kHz and 4.8 kHz, respectively. The torsional mode θ_y (sense) has resonance that is only 2% higher than the z-axis sense mode. The z-axis and θ_y sense modes are designed to be 25% higher than the x-axis drive mode. The intent is that neither the z-sense mode nor the θ_y-sense mode will be excited when the device operates at the x-axis drive resonance. Further suppression of the θ_y torsional mode at the output sense channel is provided by the fully differential capacitive interface of the accelerometer.

Fig. 10. Frequency response of the proof mass displacement with voltage applied to the x-axis drive comb fingers.

250-μm long. They consist of aluminum and oxide and have no silicon underneath, and therefore they are thin and compliant in the z-direction. Each spring branch is composed of many short beams, which increases the spring stiffness in the y-direction. Both the FEM simulation and SEM show that the thin-film z-sense spring beams bend due to residual stress, but the central plate has the same height as the frame (see Figs. 8 and 9). That is, the rotor and stator comb fingers have no vertical mismatch. The overall flatness was achieved on the whole device, and the curling present in the prior CMOS-MEMS gyroscopes [1], [2] was avoided.

The z-axis sense comb fingers are also divided into four groups to form a common-centroid configuration to reduce the cross-axis sensitivity and compensate the process variations. Each group has a pair of differential comb-finger subgroups to minimize the y-axis sensitivity. There are eight groups of z-axis comb drives which are used for self test (see Fig. 9).

VI. CHARACTERIZATION

A. Vibration Test

A microvision system [20] was used to study the vibration modes of the gyroscope. Vibration modes at different locations of the proof mass top surface have been studied. It was found that the three most lowest modes were x, z, and θ_x, as shown in Fig. 10. The measured spot was on the proof mass and is indicated by a "*" in Fig. 9, where 18-V dc and 5-V ac were applied to the x-axis comb drives. The x-axis drive mode has a resonant frequency of 3.0 kHz, and a mechanical Q-factor of 45. The resonant frequency is smaller than the nominal 3.9 kHz, which is caused by the over-undercut of the silicon underneath the drive spring beams. A measurable amount of motion is coupled to the orthogonal y-axis at resonance, however, outside of resonance the y-axis motion is below the resolution of the microvision system. The coupled z-axis motion is large (about 3% of the drive amplitude at resonance), which implies that there is an alignment mismatch between the drive stator and rotor comb fingers, which is caused by excessive undercut of silicon on the drive comb fingers. The first two sense modes, i.e., z and θ_x, were also detected, which are 5.3 kHz and 6.6 kHz, respectively.
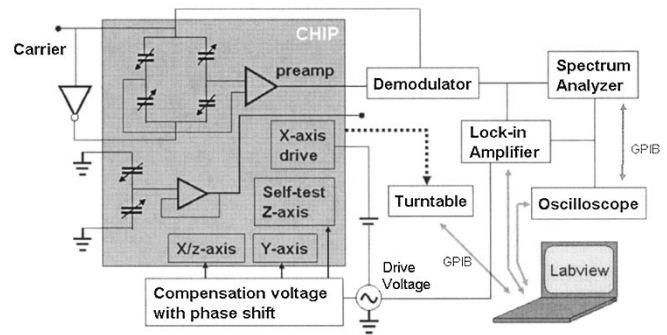

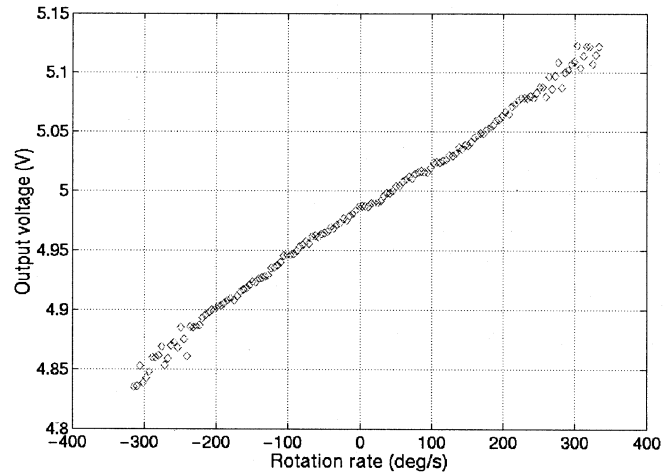Fig. 11. Test setup for characterizing the DRIE gyroscope.

Fig. 12. Static rotation rate sweep. A large dc offset and a small offset drift are present.
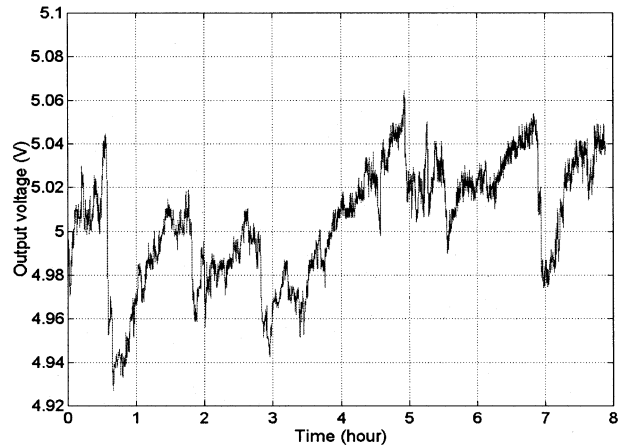

Fig. 13. Zero-rate output drift.

The 3-dB bandwidths of these two out-of-plane modes are much larger than the x-axis drive modes. The larger damping in the out-of-plane modes results from the large number of long, thick sense comb fingers. In contrast, the drive comb fingers have only 3-μm overlap.

The θ_y mode was not present in Fig. 10 when the x-axis comb drive excitation was used. The θ_y mode was observed when a voltage was applied to the x/z-axis comb drives (configured for z-axis actuation). The resonance of the θ_y mode was 4.7 kHz at 5 V ac plus 18 V dc It is even slightly lower than the z-axis sense mode.
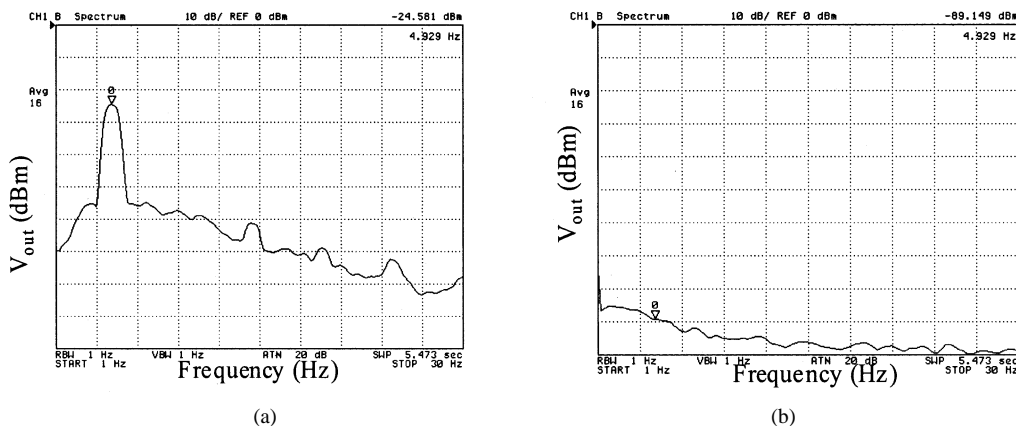
Fig. 14. Spectrum of the output signal. (a) At 5 Hz 33°/s rotation. (b) At zero rotation.

B. Rotation Test

The setup for rotation test is shown in Fig. 11. A sinusoidal voltage signal (5 V) plus a 18 V dc offset is applied to the drive comb fingers of the gyroscope. The frequency of the ac voltage is exactly the resonant frequency of the drive mode, i.e., 3.0 kHz. The device operates at atmospheric pressure. The turntable (Ideal Aerosmith Inc.) provides a rotation rate up to 360°/s. A LM1496 balanced modulator-demodulator is used to perform the first demodulation of the signal from the carrier. A lock-in amplifier (Stanford Research, Model SR830 DSP) is used for the second demodulation to extract the rotation signal from the Coriolis signal. For measurement, Labview is used to control timing, change parameters, acquire waveforms and collect data automatically from the instruments.

Since the sense capacitance is only about 0.1 pF, on-chip preamplifiers must be integrated. The employed preamplifier has a cascode topology to achieve low input capacitance and low noise. The dc bias voltages of the preamplifier inputs are set by two small transistors operating at their subthreshold regions [22].

In order to check the linearity of the device, measurement of output voltage versus rotation rate is performed from $-320°/s$ to $+320°/s$. The result is plotted in Fig. 12, where the data was acquired automatically in 12.5 min using Labview. The sensitivity is about 0.4 mV/°/s. Notice that there is a large dc offset present in the signal due to the coupled motion from the excitation vibration. This offset can be set to zero by tuning the phase of the carrier signal for the lock-in amplifier, but doing so will also significantly reduce the rotation sensitivity.

A zero-rate output (ZRO) drift over 8 h is plotted in Fig. 13. The peak-to-peak drift voltage is 100 mV, which converts to 31°/h. This large is believed to be due to the open loop operation and no temperature compensation in the system.

Since the turntable available for the experiment provides only steady rotation rate, a dc motor is used to generate a sinusoidal rotation signal. The printed-circuit board holding the gyroscope package is vertically mounted on the dc motor. The device operates at 3 kHz with ac amplitude of 5 V and dc offset of 18 V. The modulation signal is a 1-V 200-kHz square wave.

The spectrum of the output signal is shown in Fig. 14(a), where the dc motor rotates sinusoidally at 5 Hz with an amplitude of 33°/s (calibrated by the turntable). Several harmonics of 5 Hz

TABLE V
Y-AXIS COUPLED MOTION REDUCTION BY COMPENSATION

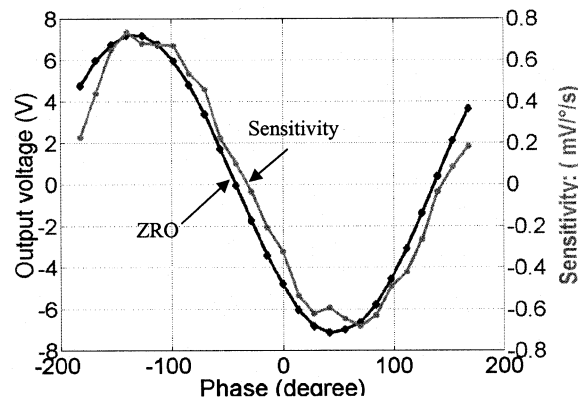|	Phase	Coupled motion reduction
self-test z-axis actuator	70±5°	10 dB
x/z-axis actuator (z)	0	4 dB
x/z-axis actuator (x)	0	8 dB

Fig. 15. Phase relation between ZRO and rotation sensitivity.

are clearly shown. There is also a broad range of low frequency spectrum present due to the vibration of the printed-circuit board. Fig. 14(b) shows the spectrum of the output signal at zero rotation. Comparing Fig. 14(a) and (b), the 33°/s rotation signal is $(-24.58 + 89.15) = 64.57$ dB above the noise floor at a bandwidth of 1 Hz, i.e., the equivalent noise floor is $0.02°/s/Hz^{1/2}$. The calculated Brownian noise is $0.01°/s/Hz^{1/2}$, with consideration of the noise folding due to the modulation. The on-chip electronics noise is estimated to be 10 nV/Hz$^{1/2}$, which is equivalent to $0.005°/s/Hz^{1/2}$. The Brownian noise is the dominant noise source. The rest of noise is almost equally from the on-chip electronics and the off-chip circuits.

All the comb drives for off-axis motion compensation are electrically grounded in the above experiments. However, some experiments were also performed by using these comb drives to reduce the coupled motion in the sense mode (along the y-axis). The results are listed in Table V. The phase in the table refers to the phase delay of the compensation voltage with respect to the primary x-axis drive voltage. The compensation voltage was set to 5-V ac plus 15-V dc.

An experiment was also conducted to study the coupled motions. Since quadrature is in phase with the primary vibration, there is a 90° phase lag between the quadrature and the Coriolis signal, according to (1). The quadrature motion signal can be suppressed and the Coriolis signal enhanced by tuning the phase of the demodulator. The phase dependences of the zero-rate output (ZRO) and the rotation sensitivity of the gyroscope are plotted in Fig. 15. The 12° phase lag between the ZRO and Coriolis signal indicates that the direct-coupled motion dominates the quadrature motion in the operation of this device [21].

Electrostatic force generated by a comb drive exists in all three directions due to small offsets. There is a 90° phase difference between drive motion along the primary actuation axis and motion generated along the z-axis because the lateral drive resonance which is much lower than the resonance of the outer frame z-axis mode. Therefore the output signal is a combination of the direct coupled z-axis motion and quadrature motion.

VII. CONCLUSION

A DRIE lateral-axis vibrating gyroscope with out-of-plane capacitive sensing was demonstrated by using a DRIE CMOS-MEMS process. The successful function of the lateral-axis gyroscope implies the feasibility of making 6-DOF inertial measurement units by using the DRIE CMOS-MEMS process. With significant circuit design effort, electronics for the complete gyroscope system are able to be included on chip.

Higher resolution can be achieved by increasing the device size, however then the noise of the on-chip electronics must be reduced. Full system control and a differential vibratory topology are also required for reduction of zero-rate offset. A vertical-force cancellation technique is needed to reduce the direct coupling. The overall performance can be further improved by design optimization [22], [23].

ACKNOWLEDGMENT

REFERENCES

[1] H. Xie and G. K. Fedder, "A CMOS-MEMS lateral-axis gyroscope," in *Proc. 14th IEEE Int. Conf. Microelectromechanical Systems*, Interlaken, Switzerland, Jan. 21–25, 2001, pp. 162–165.

[2] H. Luo, X. Zhu, H. Lakdawala, L. R. Carley, and G. K. Fedder, "A copper CMOS- MEMS z-axis gyroscope," in *Proc. 15th IEEE Int. Conf. Microelectromechanical Systems*, Las Vegas, NV, Jan. 21–25, 2001, pp. 631–634.

[3] H. Xie, L. Erdmann, X. Zhu, K. J. Gabriel, and G. K. Fedder, "Post-CMOS processing for high-aspect-ratio integrated silicon microstructures," *IEEE/ASME J. Microelectromech. Syst.*, vol. 11, pp. 93–101, Feb. 2002.

[4] G. K. Fedder, S. Santhanam, M. L. Reed, S. C. Eagle, D. F. Guillou, M. S.-C. Lu, and L. R. Carley, "Laminated high-aspect-ratio microstructures in a conventional CMOS process," *Sens. Actuators A*, vol. A57, pp. 103–110, 1996.

[5] B. Boxenhorn, "Planar Inertial Sensor," U.S. patent no 4 598 585.

[6] P. Greiff, B. Boxenhorn, T. King, and L. Niles, "Silicon monolithic micromechanical gyroscope," in *Transducers*, San Francisco, CA, June 24–27, 1991, pp. 966–968.

[7] J. Bernstein, S. Cho, A. T. King, A. Kourepenis, P. Maciel, and M. Weinberg, "A micromachined comb-drive tuning fork rate gyroscope," in *Proc. IEEE Microelectromechanical Systems*, Fort Lauderdale, FL, Feb. 7–10, 1993, pp. 143–148.

[8] M. W. Putty and K. Najafi, "A micromachined vibrating ring gyroscope," in *Tech. Dig. Solid-State Sens. Actuator Workshop*, Hilton Head Island, SC, June 13–16, 1994, pp. 213–220.

[9] W. A. Clark, R. T. Howe, and R. Horowitz, "Surface micromachined z-axis vibratory rate gyroscope," in *Proc. Tech. Dig. Solid-State Sens. Actuator Workshop*, Hilton Head Island, SC, June 3–6, 1996, pp. 283–287.

[10] T. Juneau, A. P. Pisano, and J. H. Smith, "Dual axis operation of a micromachined rate gyroscope," in *Tranducers*, Chicago, IL, June 16–19, 1997, pp. 883–886.

[11] J. A. Geen, S. J. Sherman, J. F. Chang, and S. R. Lewis, "Single-chip surface-micromachining integrated gyroscope with 50 deg/hour root Allan variance," in *Dig. IEEE Int. Solid-State Circuits Conf.*, San Francisco, CA, Feb. 3–7, 2002, pp. 426–427.

[12] T. K. Tang *et al.*, "A packaged silicon MEMS vibratory gyroscope for microspacecraft," in *Proc. 10th IEEE Int. Conf. Microelectromechanical Systems*, Nagoya, Japan, Jan. 26–30, 1997, pp. 500–505.

[13] Y. Mochida, M. Tamura, and K. Ohwada, "A micromachined vibrating rate gyroscope with independent beams for the drive and detection modes," in *Proc. 12th IEEE Int. Conf. Microelectromechanical Systems*, Orlando, FL, Jan. 17–21, 1999, pp. 618–623.

[14] M. Lutz, W. Golderer, J. Gerstenmeier, J. Marek, B. Maihofer, S. Mahler, H. Munzel, and U. Bischof, "Aprecision yaw rate sensor in silicon micromachining," in *Transducers*, Chicago, IL, June 16–19, 1997, pp. 847–850.

[15] W. Geiger, B. Folkmer, U. Sobe, H. Sandmaier, and W. Lang, "New designs of micromachined vibrating rate gyroscopes with decoupled oscillation modes," *Sens. Actuators A*, vol. 66, pp. 118–124, 1998.

[16] K. Y. Park, H. S. Jeong, S. An, S. H. Shin, and C. W. Lee, "Lateral gyroscope suspended by two gimbals through high aspect ratio ICP etching," in *Transducers*, Sendai, Japan, June 7–10, 1999, pp. 972–975.

[17] S. Adams, J. Groves, K. Shaw, T. Davis, D. Cardarelli, R. Carroll, J. Walsh, and M. Fontanella, "A single-crystal silicon gyroscope with decoupled drive and sense," in *Proc. SPIE*, vol. 3876, 1999, pp. 74–83.

[18] T. J. Brosnihan, J. M. Bustillo, A. P. Pisano, and R. T. Howe, "Embedded interconnect and electrical isolation for high-aspect-ratio, SOI inertial instruments," in *Transducers*, Chicago, IL, June 16–19, 1997, pp. 637–640.

[19] *MEMCAD User's Manual*. Cary, NC: Coventor, http://www.coventor.com.

[20] W. Hemmert, M. S. Mermelstein, and D. M. Freeman, "Nanometer resolution of 3-D motions using video interference microscopy," in *12th IEEE Int. Conf. Microelectromechanical Systems*, Orlando, FL, Jan. 17–21, 1999, pp. 302–308.

[21] H. Xie, G. K. Fedder, Z. Pan, and W. Frey, "Phase and vibration analysis for a CMOS-MEMS gyroscope," *Int. J. Nonlinear Sci. Numer. Simulations*, vol. 3, pp. 319–324, 2002.

[22] H. Luo, G. Zhang, L. R. Carley, and G. K. Fedder, "A post-CMOS micromachined lateral accelerometer," *J. Microelectromech. Syst.*, vol. 11, pp. 188–195, 2002.

[23] C. Acar and A. Shkel, "A design approach for robustness improvement of rate gyroscopes," in *Proc. Int. Conf. Modeling and Simulation of Microsystems*, Hilton Head Island, SC, Mar. 19–21, 2001, pp. 80–83.

[24] V. A. Apostolyuk1, V. J. Logeeswaran, and F. E. H. Tay, "Efficient design of micromechanical gyroscopes," *J. Micromech. Microeng.*, vol. 12, pp. 948–954, 2002.
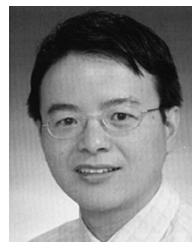
Huikai Xie received the B.S. and M.S. degrees in electronic engineering from the Beijing Institute of Technology, Beijing, China, the M.S. degree in electrooptics from Tufts University, Medford, MA, in 1998, and the Ph.D. degree in electrical and computer engineering from Carnegie-Mellon University, Pittsburgh, PA, in 2002.

He is an Assistant Professor at the Department of Electrical and Computer Engineering, University of Florida, Gainesville. From 1992 to 1996, he was a Faculty Member at the Institute of Microelectronics, Tsinghua University, Beijing, working on various silicon-based microsensors. He has published over 30 technical papers. His present research interests include integrated microsensors, optical MEMS, optical switching, biomedical imaging and sensing, and fiberoptic sensors.

Gary K. Fedder received the B.S. and M.S. degrees in electrical engineering from the Massachusetts Institute of Technology, Cambridge, in 1982 and 1984, respectively, and the the Ph.D. degree from the University of California, Berkeley, in 1994, where his research resulted in the first demonstration of multimode control of a underdamped surface-micromachined inertial device.

He is currently a Professor at Carnegie-Mellon University, Pittsburgh, PA, holding a joint appointment with the Department of Electrical and Computer Engineering and The Robotics Institute. From 1984 to 1989, he was with the Hewlett-Packard Company, working on circuit design and printed-circuit modeling. He serves on the editorial board of the IOP *Journal of Micromechanics and Microengineering* and as coeditor of the Wiley-VCH *Sensors Update* book series. He has contributed to over 90 research publications and several patents in the MEMS area. His research interests include microsensor and microactuator design and modeling, integrated MEMS manufactured in CMOS processes, and structured design methodologies for MEMS.

Dr. Fedder received the 1993 AIME Electronic Materials Society Ross Tucker Award, the 1996 Carnegie Institute of Technology G.T. Ladd Award, and the 1996 NSF CAREER Award. Currently, he serves as a subject Editor for the IEEE/ASME Journal of Microelectromechanical Systems,